

Report Number 11/01

**Improving the efficiency of optical coherence tomography by using
the non-ideal behaviour of a polarising beam splitter**

by

Norman Lippok, Poul Nielsen, and Frederique Vanholsbeeck



Oxford Centre for Collaborative Applied Mathematics
Mathematical Institute
24 - 29 St Giles'
Oxford
OX1 3LB
England

Improving the efficiency of optical coherence tomography by using the non-ideal behaviour of a polarising beam splitter

¹Norman Lippok, ¹Poul Nielsen, and ²Frédérique Vanholsbeeck

¹Auckland Bioengineering Institute, ²Physics Department, The University of Auckland,
Private Bag 92019, Auckland, New Zealand

n.lippok@auckland.ac.nz

Abstract: We present a new way of improving the efficiency of optical coherence tomography by using the polarisation crosstalk of a polarising beam splitter to direct most of the available source optical power to the sample. The use of a quarter wave plate in both the reference and the sample arms allows most of the sample power to be directed to the detector while adjusting the reference arm to ensure noise optimised operation. As a result, the sensitivity of such a system can be improved by 6 dB, or alternatively the acquisition time can be improved by a factor of 4 for shot noise limited performance.

© 2010 Optical Society of America

OCIS codes: (110.4500)Optical coherence tomography (Imaging systems), (170.3890) Medical optics instrumentation, (230.1360) Beam splitters (Optical devices)

References and links

1. D. Huang, E. A. Swanson, C. P. Lin, J. S. Schuman, W. G. Stinson, W. Chang, M. R. Hee, T. Flotte, K. Gregory, and C. A. Puliafito, "Optical coherence tomography," *Science* **254**, 1178-1181 (1991).
2. A. F. Fercher, C. K. Hitzenberger, G. Kamp, S.Y. El-Zaiat, "Measurement of intraocular distances by backscattering spectral interferometry," *Opt.Commun.* **117**, 43-48 (1995).
3. G. Haeusler, M. W. Lindner, "Coherence radar and spectral radar - New tools for dermatological diagnosis," *J. Biom. Opt.* **3**(1), 21-31 (1998).
4. R. Huber, M. Wojtkowski, and J. G. Fujimoto, "Fourier Domain Mode Locking (FDML): A new laser operating regime and applications for optical coherence tomography," *Opt. Express* **14**, 3225-3237 (2006).
5. R. Leitgeb, C. K. Hitzenberger, A. F. Fercher, "Performance of fourier domain vs. time domain optical coherence tomography," *Opt. Express* **11**, 889-894 (2003).
6. W. V. Sorin, D. M. Baney, "A Simple Intensity Noise Reduction Technique for Optical Low-Coherence Reflectometry," *IEEE Photonics Technology Letters* **4**, 1404-1406 (1992).
7. A. M. Rollins, J. A. Izatt, "Optimal interferometer designs for optical coherence tomography," *Opt. Letters* **24**, 1484-1486 (1999).
8. B. M. Hoeling, A. D. Fernandez, R. C. Haskell, E. Huang, W. R. Myers, D. C. Petersen, S. E. Ungersma, R. Wang, M. E. Williams, S. E. Fraser, "An optical coherence microscope for 3-dimensional imaging in developmental biology," *Opt. Express* **6**, 136-146 (2000).
9. G. Tearney, S. A. Boppart, B. E. Bouma, M. Brezinski, E. A. Swanson, J. G. Fujimoto, "Method and apparatus for performing optical measurements using a fiber optic imaging guidewire, catheter or endoscope," US Patent No. 6,134,003 (1996).
10. C. K. Hitzenberger, "Efficient optical coherence tomography (OCT) system and method for rapid imaging in three dimensions," US Patent No. 2005/0140984 A1 (2005).
11. E. Beaurepaire, A. C. Boccara, M. Lebec, L. Blanchot, H. Saint-Jalmes, "Full-field optical coherence microscopy," *Opt. Letters* **23**, 244-246 (1998).

12. A. Dubois, L. Vabre, A. C. Boccara, E. Beaurepaire, "High-resolution full-field optical coherence tomography with a Linnik microscope," *Applied Optics* **41**, 805-812 (2002).
 13. E. Collett, *Polarized light: fundamentals and applications* (Marcel Dekker, New York, 1993).
 14. M. Wojtkowski, V. J. Srinivasan, T. H. Ko, J. G. Fujimoto, A. Kowalczyk, J. S. Duker, "Ultra-high-resolution, high-speed, Fourier domain optical coherence tomography and methods for dispersion compensation," *Opt. Express* **12**, 2404-2422 (2004).
 15. M. A. Choma, M. V. Sarunic, C. Yang, J. A. Izatt, "Sensitivity advantage of swept source and Fourier domain optical coherence tomography," *Opt. Express* **11**, 2183-2189 (2003).
 16. W. Wieser, B. R. Biedermann, T. Klein, C. M. Eigenwillig, and R. Huber, "Multi-Megahertz OCT: High quality 3D imaging at 20 million A-scans and 4.5 GVoxels per second," *Opt. Express* **18**, 14685-14704 (2010).
-

1. Introduction

Optical coherence tomography (OCT) is a real-time non-invasive imaging technique that produces high resolution, cross sectional images of biological tissues [1]. It is based on low coherence interferometry. Accordingly, the axial resolution is inversely proportional to the bandwidth of the light source. Originally, reflections in the sample arm were scanned in the time domain by using a variable time delay in the reference arm so as to move the source coherence gate through the sample [1]. More recently, OCT imaging has shifted to spectral domain operation by using a spectrometer [2,3] to acquire the interferometric signal, or by using a wavelength swept source [4].

Even though the interest in OCT has grown considerably over the last two decades, most OCT systems still waste a significant portion of their optical power. OCT systems are typically designed around either a Michelson or a Mach-Zehnder interferometer. They usually present minimal intrinsic losses in the reference arm of the interferometer while the sample arm reflectivity can be, for biological samples, up to four orders of magnitude smaller than that of a perfect reflector. In the Mach-Zehnder configuration, it is in principle possible to unevenly split the power of the light source between the two arms of the interferometer to overcome this loss imbalance. However, a 50/50 beam-splitter (BS) is still required in the sample arm to direct the light towards the sample and collect the reflected signal, thereby resulting in a 75 % loss. Typical Michelson interferometers guide equal power to the sample and the reference arm, but after recombination only 50 % of the light coming from both arms is directed towards the detector, whereas the other half is sent back to the source and lost. Consideration must also be given to the acquisition speed of the OCT system, which depends on the sensitivity, the signal to noise ratio (SNR), and the dynamic range. Typically, the dynamic range is much smaller than the sensitivity, and the reference power has to be attenuated by a factor of 100 or more to improve the detector SNR and to avoid working in the excess intensity noise regime [5–8]. Overall, in all these designs, more than 75 % of the source power is lost, which is highly inefficient.

An efficient OCT system would incorporate reference arm power attenuation for optimum noise performance without losing the available source power, and instead divert more light to the sample. By increasing the power delivered to the sample, such a system would improve the OCT sensitivity as well as the scanning speed for existing source power levels. Several approaches to achieve this goal have been suggested. Rollins *et al* considered interferometer designs based on optical circulators to avoid the loss associated with the traditional use of 50/50 BSs [7]. However, circulators for near-infrared OCT wavelengths are not widely available, are expensive, and lossy. OCT systems taking advantage of the polarisation properties of light have also been trialled with the aim of directing all the light coming back from the reference and sample arms toward the detector. Tearney *et al* [9] used a Faraday rotator in a fibre optic design, but such rotators are expensive. Hitzenberger *et al* [10] used a combination of a polariser and a polarising beam splitter (PBS) to adjust the reference signal to a low level while guiding all the remaining source power toward the sample. By carefully adjusting the

polariser, one can avoid operating the detector in the excess noise and receiver noise domain, with a theoretical sensitivity improvement of 5.5 dB for the available source power. Similar approaches, combined with signal modulation techniques for complete image reconstruction, have also been used by other groups [11, 12]. Despite this, with all these methods, the reference and sample signals emerge from the interferometer with orthogonal polarisation states. Therefore, an analyser is required at the output to get the interferometric signal, which again leads to further attenuation.

Here, we propose a new way of using a PBS to improve the sample signal level, and thus the SNR for Michelson or Mach-Zehnder OCT configurations and avoid both the excess intensity noise and receiver noise regimes. While experimental verification is made with a Fourier-domain (FD) OCT system, most of our results can be easily transposed to time-domain (TD) or swept-source OCT systems. Our approach is based on the polarisation cross-talk ratio of a non-ideal PBS. In the next Section, we start by introducing the theory of polarisation cross-talk. Section 3 will be devoted to the description and the characterisation of the configurations. The results are then discussed in Section 4 and finally the conclusions will be drawn in Section 5.

2. Theory

To enhance the efficiency of our OCT system, and thus its sensitivity as well as its acquisition speed, we use the non ideal behaviour of real PBSs, and in particular the fact that their extinction ratio is not 100 %. The extinction ratio of a PBS is, for each output direction, the ratio of the power in the expected polarisation state over that of the light with the unwanted polarisation. The extinction ratio is generally different for both PBS directions and typically lies between 20 dB and 30 dB. The notion of extinction ratio naturally leads to the concept of polarisation crosstalk as it implies that some of the p (s) polarised light that is normally transmitted through (reflected by) the PBS leaks in the reflected (transmitted) beam, respectively. The polarisation cross-talk ratio r_σ is defined as

$$r_\sigma = \frac{P'_\sigma}{P_\sigma}, \quad (1)$$

where P_σ and P'_σ are the optical powers of the beams in the supported and unsupported (leaking) direction of the PBS for a given polarisation state ($\sigma = p$ or s). Recall that the p-polarised light is defined as the light that has a polarisation parallel to the plane formed by the propagation direction of the beam incident on the PBS and the normal to the incidence surface, while the s-polarised light is polarised in the orthogonal direction. We have measured the polarisation crosstalk ratio of two PBSs from two different distributors (Newport and Casix) and the results are reported in Table 1. Note that the resolution and the background noise of our measurement system prevented any more accurate measure of the s-polarisation crosstalk ratio of the Newport PBS that is below -27 dB.

We now consider a PBS in a Michelson interferometer in which a mirror is placed in the reflected direction to constitute the reference arm of an OCT configuration as seen in Fig. 1. By using the polarisation crosstalk of the PBS and a p-polarised light source, it is therefore

Cross Talk Ratio	Newport	Casix
r_p [dB]	-20.4 (1.6)	-10.1 (0.7)
r_s [dB]	< -27	-21.8 (1.7)

Table 1. Measurements of crosstalk ratios for PBSs from two different distributors in the transmission (p) and the reflection (s) directions. Numbers in bracket represent standard deviation.

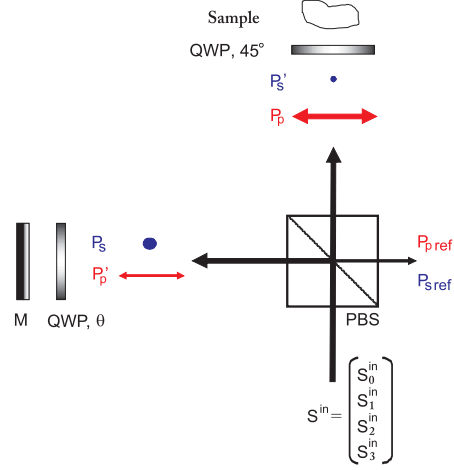


Fig. 1. Polarising beam splitter (PBS), the p-polarised light is transmitted while the s-polarised is reflected to the reference arm where a mirror and quarter wave plate (QWP) with an angle θ of fast optical axis are placed.

possible to direct a very small portion r_p , between -20 dB to -30 dB, of the incident light towards the reference arm. Interestingly, this reference signal is p-polarised (it has the same polarisation state as the signal beam). Hence, after reflection from the reference mirror, the PBS will direct it towards the detector without incurring further loss. In fact, the smallness of the crosstalk reduces the need for further attenuation of the reference signal. In practice, it is still advantageous to place a quarter wave plate (QWP) in the reference path. Adjusting the orientation of that QWP enables the power of the reference signal to be fine-tuned for optimum detection noise.

To investigate this approach in more detail, in the following we calculate the power of the reference signal using Stokes parameters and Mueller matrices [13]. We use the Mueller formalism to allow us to take into account the wavelength dependence of our optical elements for better comparison with the experiments. Also, to make our calculations more general, we initially assume that the polarisation state incident on the PBS is arbitrary, and defined by its Stokes vector $\mathbf{S}^{\text{in}} = (S_0^{\text{in}}, S_1^{\text{in}}, S_2^{\text{in}}, S_3^{\text{in}})^T$.

For each polarisation component, and in each output direction, the PBS can be represented by a linear polariser multiplied by an attenuation coefficient, taking into account the effect of the polarisation crosstalk as defined by Eq. (1). We will denote the Mueller matrices for these polarisers as M_σ (where $\sigma = p, s$). They read [13]

$$M_\sigma = \frac{1}{2} \begin{bmatrix} 1 & \pm 1 & 0 & 0 \\ \pm 1 & 1 & 0 & 0 \\ 0 & 0 & 0 & 0 \\ 0 & 0 & 0 & 0 \end{bmatrix}. \quad (2)$$

where the $+$ ($-$) sign refers to the p (s) polarisation, respectively. Note that in our system, the p-wave (s-wave) is horizontally (vertically) polarised. It follows that the Stokes parameters of the beams in the supported and unsupported directions of the PBS, for each polarisation state, can be written as

$$\mathbf{P}_\sigma = \frac{1}{1+r_\sigma} M_\sigma \mathbf{S}^{\text{in}}, \quad (3)$$

$$\mathbf{P}'_\sigma = r_\sigma \mathbf{P}_\sigma = \frac{r_\sigma}{1+r_\sigma} M_\sigma \mathbf{S}^{\text{in}}. \quad (4)$$

The optical power of each signal component is the first element of the vectors \mathbf{P}_σ and \mathbf{P}'_σ . Using Eq. (2), the above equations can be expressed in terms of the input Stokes parameters $S_{0,1,2,3}^{\text{in}}$ as

$$\mathbf{P}_\sigma = \frac{S_0^{\text{in}} \pm S_1^{\text{in}}}{2} \frac{1}{1+r_\sigma} \mathbf{S}_\sigma, \quad (5)$$

$$\mathbf{P}'_\sigma = \frac{S_0^{\text{in}} \pm S_1^{\text{in}}}{2} \frac{r_\sigma}{1+r_\sigma} \mathbf{S}_\sigma, \quad (6)$$

where $\mathbf{S}_\sigma = (1, \pm 1, 0, 0)^T$ is a unitary Stokes vector representing the p (+) and s (-) polarisation states. With these notations, the beam launched in the reference arm of our OCT system, which is in the reflected direction of the PBS (see Fig. 1), is therefore represented by the Stokes vector $\mathbf{P}_s + \mathbf{P}'_p$.

The QWP in the reference arm of our OCT system can similarly be described using the Mueller formalism. Let M_{QWP} be the Mueller matrix of a QWP with a fast axis oriented along the direction of the electric-field of the p-polarisation state. A QWP with an arbitrary orientation θ with respect to that direction can then be described by the product $M_{\text{R}}(-\theta)M_{\text{QWP}}M_{\text{R}}(\theta)$, where M_{R} is an appropriate rotation matrix. The required matrices are expressed as [13]

$$M_{\text{WP}}(\delta) = \begin{bmatrix} 1 & 0 & 0 & 0 \\ 0 & 1 & 0 & 0 \\ 0 & 0 & \cos(\delta) & -\sin(\delta) \\ 0 & 0 & \sin(\delta) & \cos(\delta) \end{bmatrix}, \quad M_{\text{R}}(\theta) = \begin{bmatrix} 1 & 0 & 0 & 0 \\ 0 & \cos(2\theta) & \sin(2\theta) & 0 \\ 0 & -\sin(2\theta) & \cos(2\theta) & 0 \\ 0 & 0 & 0 & 1 \end{bmatrix}. \quad (7)$$

Here we have given the general expression $M_{\text{WP}}(\delta)$ for a wave plate of arbitrary retardance δ , where $M_{\text{QWP}} = M_{\text{WP}}(\pi/2)$. After passing through the QWP, the reference beam hits a reflector before going through the QWP a second time. As an ideal reflector at normal incidence only changes the signs of the S_2 and S_3 components of the Stokes vector, the double pass in the QWP including the mirror reflection can therefore be written as $M_{\text{R}}(-\theta)M_{\text{QWP}}^2M_{\text{R}}(\theta)$.

Taking into account a further transmission through the PBS via Eqs. (3)–(4), the Stokes vector of p- and s-polarised reference beams that eventually reach the detector are then expressed as

$$\begin{aligned} \mathbf{P}_{\text{p,ref}} &= \alpha_{\text{L}} \left[\frac{1}{1+r_{\text{p}}} M_{\text{p}} \right] [M_{\text{R}}(-\theta)M_{\text{QWP}}^2M_{\text{R}}(\theta)] (\mathbf{P}_s + \mathbf{P}'_p) \\ &= \frac{\alpha_{\text{L}}}{1+r_{\text{p}}} \left[\frac{S_0^{\text{in}} - S_1^{\text{in}}}{2(1+r_{\text{s}})} \sin^2(2\theta) + r_{\text{p}} \frac{S_0^{\text{in}} + S_1^{\text{in}}}{2(1+r_{\text{p}})} \cos^2(2\theta) \right] \mathbf{S}_{\text{p}}, \end{aligned} \quad (8)$$

$$\begin{aligned} \mathbf{P}_{\text{s,ref}} &= \alpha_{\text{L}} \left[\frac{r_{\text{s}}}{1+r_{\text{s}}} M_{\text{s}} \right] [M_{\text{R}}(-\theta)M_{\text{QWP}}^2M_{\text{R}}(\theta)] (\mathbf{P}_s + \mathbf{P}'_p) \\ &= \frac{\alpha_{\text{L}} r_{\text{s}}}{1+r_{\text{s}}} \left[\frac{S_0^{\text{in}} - S_1^{\text{in}}}{2(1+r_{\text{s}})} \cos^2(2\theta) + r_{\text{p}} \frac{S_0^{\text{in}} + S_1^{\text{in}}}{2(1+r_{\text{p}})} \sin^2(2\theta) \right] \mathbf{S}_{\text{s}}. \end{aligned} \quad (9)$$

Here \mathbf{P}'_p and \mathbf{P}_s are defined in Eqs. (5) and (6) and α_{L} is a coefficient that accounts for the linear losses induced by the optical components of the system, such as reflection, absorption, and insertion losses. In normal operation of our OCT system, only p (i.e., horizontally) polarised light is incident on the PBS ($\mathbf{S}^{\text{in}} = P_0 \mathbf{S}_{\text{p}}$) and the first term inside the brackets in each of the above equations vanishes ($S_0^{\text{in}} = S_1^{\text{in}}$). The powers coming from the reference arm then simplify as

$$P_{\text{p,ref}} = \frac{\alpha_{\text{L}} r_{\text{p}}}{(1+r_{\text{p}})^2} P_0 \cos^2(2\theta) \quad (10)$$

$$P_{\text{s,ref}} = \frac{\alpha_{\text{L}} r_{\text{s}} r_{\text{p}}}{(1+r_{\text{s}})(1+r_{\text{p}})} P_0 \sin^2(2\theta) \quad (11)$$

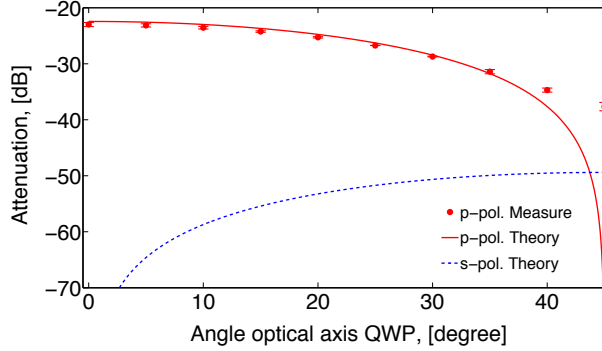


Fig. 2. Theoretical optical attenuation of the reference signal in dB for both p (solid) and s (dashed) polarisation states as a function of the angle θ between the fast-axis of the QWP and the horizontal, based on Eqs. (10) and (11). Dots represent experimentally measured values for the p-polarisation.

where P_0 is the total power launched in the interferometer.

To illustrate the significance of these relations, we have plotted in Fig. 2 the reference beam optical attenuation $P_{\sigma,\text{ref}}/P_0$ in dB for both polarisation components as a function of the orientation θ of the QWP. Here we have used the crosstalk coefficients of the Newport PBS (see Table 1). In this configuration, the reference beam is predominantly p-polarised. Fig. 2 also demonstrates that, by rotating the QWP in the reference arm, the reference beam can be attenuated continuously in a range ideal for OCT, with the minimum attenuation given by the p-polarisation cross talk ratio r_p . We have compared these calculations with measurements using the arrangement shown in Fig. 1. An analyser was used at the PBS output to select the p- or s-polarisation states. Although the s-polarised reference light ($P_{s,\text{ref}}$) was not accessible because of polarisation crosstalk noise between the axes of the PBS at such high attenuations, the agreement is excellent for the p-polarisation state. The cross talk noise between the orthogonal polarization states was found to be at -40 dB. As the p-polarization state approaches such high attenuation, the measurements for the p-polarized light depart from our analytical expression (Eq. 10).

3. Methods

3.1. QWP characterisation and signal attenuation

As seen in Fig. 2, the polarisation crosstalk ratio of a PBS can be used to efficiently attenuate the reference signal in order to optimise the noise performance of an OCT system. However, it is still important to select high quality optical components to maximise the efficiency of our system. In particular, the QWP should be broadband to ensure that the optical spectrum is not altered due to the frequency dependence of the wave-plate retardation, and that no optical power is lost when passing through the PBS. For that reason, we have used an achromatic Quartz-MgF2 Zero-Order QWP (Newport, 10RP54-2) that is constructed from two different birefringent crystals, crystalline quartz and magnesium fluoride (MgF2), that can operate over the 700 nm to 1000 nm wavelength range. A wavelength-dependent measurement (using a polarimeter) for p-polarised light incident on the QWP shows that the retardance does not deviate from $\lambda/4$ by more than 0.0012 waves over a 100 nm bandwidth [solid line in Fig. 3(a)]. In comparison, the retardance of polymer or quartz-only zero-order QWPs deviate significantly more over the same bandwidth [dashed and dotted curves in Fig. 3(a)].

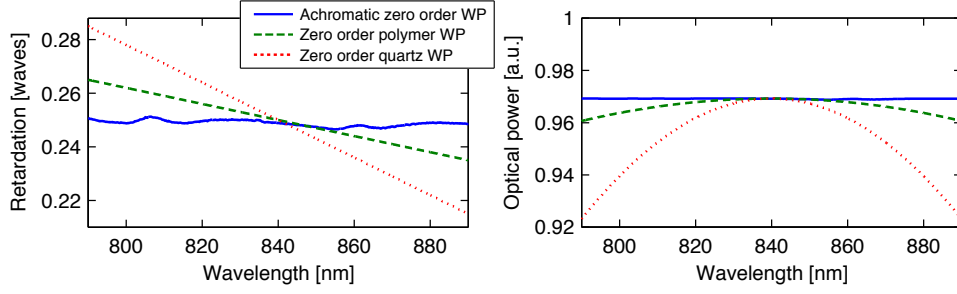


Fig. 3. (a) Retardation angle as a function of wavelength for the achromatic zero-order QWP (plain line), compared with standard zero-order QWP. (b) Modelled optical power after double pass through the QWP characterised in (a) and the PBS at the interferometer output.

We now focus our attention on the sample arm. From the above discussion, it should be clear that the light entering the sample arm is p-polarised. Therefore, if the sample does not present any optical activity, another QWP oriented at 45° must be placed in the sample arm to convert the sample light to s-polarised light so that, on the return path, it is reflected by the PBS and entirely directed towards the detector. This is necessary to ensure the signal loss is minimal. At the detector, the signal polarisation will then be orthogonal to the predominantly p-polarised reference light (see Fig. 2) and will not interfere with it. In the past, an analyser has been used to solve that issue but we will show later in this paper how we have addressed this differently. Using the measured characteristics of our QWP, we have calculated the Stokes parameters of the s-polarised signal beam $\mathbf{P}_{s,\text{sample}}$ after double pass through the QWP and the PBS to predict the wavelength dependant signal losses in the system presented in Fig. 1. Assuming a perfect reflector as sample, the Stokes parameters at the interferometer output can be calculated using the same approach as the one that led to Eqs. (5) and (6),

$$\mathbf{P}_{s,\text{sample}} = \frac{\alpha_{\text{mirror}}\alpha_{\text{PBS}}}{(1+r_p)(1+r_s)} M_s M_R(-\theta) M_{\text{WP}}^2(\delta) M_R(\theta) M_p \mathbf{S}^{\text{in}}. \quad (12)$$

where $\mathbf{S}^{\text{in}} = P_0 \mathbf{S}_p$, $\theta = \pi/4$, and with δ the measured retardance of our QWP as shown in Fig. 3(a). α_{mirror} is the sample mirror reflection coefficient and α_{PBS} is the PBS transmission as specified by the manufacturer. The first component of the sample output Stokes vector given by Eq. (12) gives the output power. After normalisation by the incident power P_0 , we obtain the wavelength-dependent sample arm transmission for our system. This is plotted in Fig. 3(b) as the solid curve. The predicted mean power loss in the sample arm is 3.1% and, given its uniformity over our 100 nm bandwidth, is mainly due to the losses induced by the mirror and the PBS, including those due to the polarisation cross-talk, rather than the non-ideal QWP retardation. This latter point is highlighted by the dashed and dotted curves in Fig. 3(b) that have been calculated for the polymer and quartz-only zero-order QWPs whose characteristics are plotted in Fig. 3(a). An experimental measurement performed with the achromatic Quartz-MgF2 zero-order QWP revealed a mean power loss of 3.6%, in agreement with the theoretical mean value. This shows that more than 96% of the input light can be efficiently guided to the sample and back to the detector using our system and a mirror as sample. This is four times more optical power than standard designs based on a 50/50 BS [Fig. 4(a)].

3.2. Lossless interferometric mixing

In summary, using a p-polarised source and the polarisation cross-talk ratio of the PBS, we can obtain an s-polarised sample beam carrying most of the optical power and a p-polarised reference beam at a level of -20 dB or lower. In the past, a similar result has been achieved with an input polariser in front of the PBS. The optical power ratio between the sample and the reference arm was then adjusted by tuning the orientation of the input polariser [11, 12]. Previous experiments also used an output analyser placed after the PBS to get the interferometric signal. Adjusting the relative orientation of the input polariser and output analyser maximised sample illumination and OCT efficiency [10]. Clearly, rotating the analyser to favour the sample arm power level increases the sensitivity. However, this leads to supplemental power loss for the signal beam.

To avoid loss of the signal in our polarisation cross-talk-based scheme, we have inserted a second PBS in the reference arm as shown in Fig. 4(b). In this way, we now extract s-polarised light from the reference arm with a power given by $P_{s,ref} = \alpha_L r_p P_0 \sin^2(2\theta) / [(1 + r_s)(1 + r_p)^2]$. By doing so, and by rotating the QWP of the reference arm by 45° , we essentially swap the p- and s-polarised beams in Fig. 2. The minimum reference beam attenuation is still given approximately by the p-polarisation cross-talk ratio r_p , and we still have the same flexibility to adjust the reference power to a suitable level. The key difference, however, is that the reference beam extracted this way has now the same polarisation as the signal beam outputting the first PBS. An analyser at the output of what is now a Mach-Zhender interferometer is therefore not required, allowing *all* the sample light to be used for maximum efficiency. Clearly, this configuration provides minimal losses for both the reference and sample arm, and most of the source power ($> 96\%$) is sent to the sample and redirected to the detector. In the rest of this paper, the performance of this scheme will be evaluated and compared to a standard OCT system as presented in Fig. 4 (a).

We can now complete the description of our configuration, which is shown in full in Fig. 4(b). The light source provides an optical bandwidth of 70 nm, centred at 822 nm. The sample is positioned in front of a galvanometer mirror stage (Cambridge Technology) for transverse scanning, and a 75 mm focal length lens focuses the beam onto the sample. An identical lens is incorporated into the reference arm to balance dispersion. The two PBSs are made of different materials with the principal PBS presenting more dispersion than the reference arm PBS. As a result, the double pass in the reference arm PBS induces less dispersion than a single-pass in

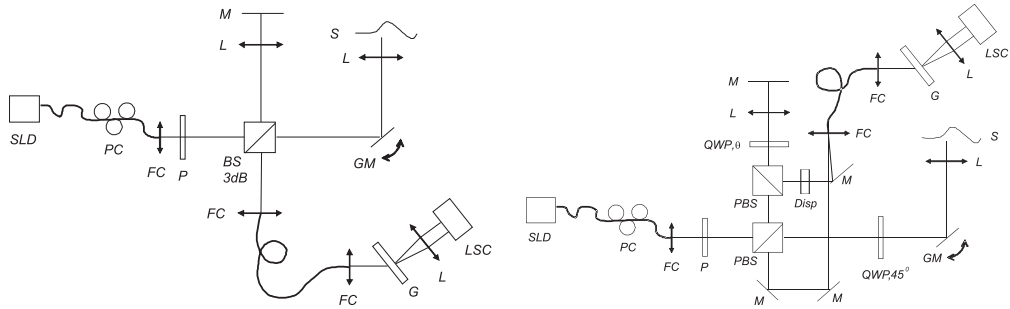


Fig. 4. (a) OCT1: Standard OCT system based on a Michelson interferometer. (b) OCT2: Efficient OCT system using PBS crosstalk ratio. In these figures, SLD: superluminescent diode, PC: polarisation controller, P: polariser, A: analyser, BS 3dB: 50/50 beam splitter, PBS: polarising beam splitter, L: lens, M: mirror, GM: galvanometer mirror, S: sample, Disp: dispersion compensation, G: grating, and LSC: line scan camera.

the principal PBS. To compensate for second order dispersion, an additional dispersive element has been included in the reference arm. Third order dispersion was neglected.

The two configurations that we compare in this paper are FD-OCT systems, and for detection use the same custom built spectrometer. At the exit of the interferometer, the reference and sample light were overlapped onto the tip of a single-mode fibre, which acted as a spatial filter at the spectrometer input. As seen in Fig. 4 (b), the reference beam was launched slightly off-axis in the spectrometer input fibre. This reduced the reference beam in-fibre coupling efficiency to $< 20\%$ but was sufficient to saturate the pixels of the spectrometer with an integration time of $\sim 40 \mu\text{s}$. The light emitted from the fibre end was collimated by an achromatic doublet lens with a 30 mm focal length before being spectrally dispersed by a transmission volume phase holographic grating (1200 lines/mm, Wasatch Photonics Inc.) and imaged onto a CMOS line scan camera (BASLER Sprint spl2048-70km) using another achromatic doublet lens with 200 mm focal length. The camera provided 2048 pixels, 12 bit resolution, and a maximum acquisition rate of 70 kHz.

To achieve the optimal axial resolution possible with our source without compromising the depth measurement range, we should ideally use a spectrometer bandwidth of 158 nm [14]. As the bandwidth of our spectrometer was limited to 93 nm, the designed axial pixel spacing was slightly too large compared to the axial resolution, which degrades the sensitivity. This was neglected in this proof-of-principle demonstration as it affects equally the sensitivity of the two configurations we compare. The spectrometer efficiency, i.e., the ratio between the signal measured by the camera and the power incident on the grating, was measured to be 18%. The additional coupling through a fiber coupler at the spectrometer input further reduced it to $\rho = 11\%$.

3.3. Sensitivity

In order to show that we can achieve a sensitivity improvement by using the PBS crosstalk ratio, we define here sensitivity for a FD-OCT system as well as its noise sources. The FD-OCT A-scan peak signal amplitude can be written as [5]

$$A_{\text{FDOCT}}^{\text{Peak}} = \frac{\rho \eta \tau \lambda_0 P_0}{hc} \frac{1}{N} \sqrt{\gamma_r \gamma_s R_r R_s \Delta \gamma_r} \quad (13)$$

where τ is the exposure time, η is the detector quantum efficiency, N is the number of pixel, ρ is the spectrometer efficiency, while $R_{r,s}$ and $\gamma_{r,s}$ are, respectively, the reference (r) and sample (s) arm reflectivities and maximum achievable interferometer arm efficiencies. For practical reasons and for better comparison with the experiments, we additionally introduce the coefficient $\Delta \gamma_r$, which represents a further reduction of the reference arm optical power (efficiency). In practice, $\Delta \gamma_r$ is adjusted by rotation of the reference arm quarter wave plate, so that the reference arm optical power is tuned to saturate the camera.

The main photoelectron noise variances in FD-OCT are given by the shot noise, σ_{shot}^2 , the excess noise, σ_{excess}^2 , and the detector noise, $\sigma_{\text{receiver}}^2$ [5, 6, 15]. The total noise in FD-OCT, after performing the discrete Fourier transform on the superimposed spectral depth fringes, can be written as [5]

$$\tilde{\sigma}_{\text{noise}}^2 = \frac{1}{N} (\sigma_{\text{shot}}^2 + \sigma_{\text{excess}}^2 + \sigma_{\text{receiver}}^2) \quad (14)$$

With the signal to noise ratio (SNR) written as $\text{SNR} = \langle A_{\text{FDOCT}}^{\text{Peak}} \rangle^2 / \tilde{\sigma}_{\text{noise}}^2$, the system sensitivity (S) is defined as the minimum sample reflectivity to achieve $\text{SNR} = 1$ [5],

$$S = \frac{\frac{1}{N} \left(\frac{\rho \eta \tau \lambda_0 P_0}{hc} \right)^2 \Delta \gamma_r \gamma_r \gamma_s R_r}{\frac{\rho \eta \tau \lambda_0 P_0}{hc} \frac{1}{N} \Delta \gamma_r \gamma_r R_r \left[1 + \frac{(1+\Pi^2)}{2} \frac{\rho \eta \lambda_0 P_0 \Delta \gamma_r \gamma_r R_r \tau_{\text{coh}}}{hc} \right] + \sigma_{\text{receiver}}^2}, \quad (15)$$

where Π is the degree of polarisation of the source (assumed to be 1), and τ_{coh} is the coherence time of the source. This approximation holds only for $R_s \ll R_r$, when the noise contribution of the sample arm is negligible. This is true in most OCT applications. In our configurations, $\gamma_{r,s}$ is measured as the ratio between the power that exits the fibre at the spectrometer input and the power at the PBS input assuming $R_r = R_s = 1$. Using the PBS crosstalk ratio, we optimise γ_r and γ_s for best efficiency compared to a standard OCT system. Moreover, $\Delta\gamma_r$ can be continuously adjusted by carefully rotating the reference QWP. This allows us to avoid operating in the excess noise and receiver noise domain, while making low reflectivity measurements available for the typically low dynamic range of the spectrometer. In this case, as seen in Eq. (15), we can neglect $\gamma_s R_s$ in the denominator and the sensitivity becomes directly proportional to the sample arm efficiency, γ_s .

4. Discussion

4.1. Sensitivity improvement

We now compare experimentally the sensitivity of the two OCT configurations presented in Fig. 4, namely the standard Michelson OCT design based on a 50/50 BS [OCT1, Fig. 4(a)] and our efficient PBS-based OCT system using polarisation cross-talk [OCT2, Fig. 4(b)]. Both configurations share most of their optical components, and system losses due to reflection and transmission coefficients are only marginally higher in the efficient OCT configuration (OCT2). The system losses can be considered equal for the sample arm in both configurations. Moreover, to ensure equal measurement conditions for both configurations we maintained the same input power, same camera integration time at 5 kHz A-scan rate and same sample coupling efficiency into the single mode fibre at the spectrometer input. The use of the polarisation cross talk ratio improves γ_s by a factor of 5 for OCT2 in comparison with OCT1. This is more than the expected factor of 4, mainly because the BS in OCT1 is not truly 50/50.

To measure the sensitivity, a perfect reflector was used as the sample, and the reference arm power level is initially adjusted such that the spectrum measured with the CMOS camera is close to saturation level for a given integration time. Subsequently, a neutral density filter presenting a double pass attenuation of 60 dB ($D = 3$) was placed into the sample arm. The sensitivity S in dB was then calculated as 20 times the \log_{10} of the ratio between the A-scan peak amplitude and the rms noise value, to which we add 60 dB, i.e., the sample arm attenuation. The noise level measurement was taken at the location of the A-scan peak after blocking the sample arm. For each measurement, the reference arm signal, measured by blocking the sample arm,

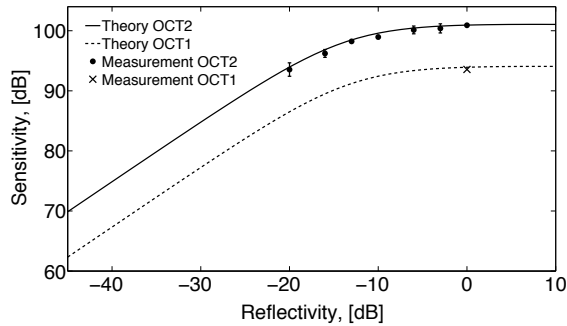


Fig. 5. Sensitivity versus reference arm reflectivity R_r . The theoretical prediction is based on Eq. (15) while the data points are experimental and correspond for both systems to sensitivity measurements at 5 kHz A-scan rate and a depth of 100 μm .

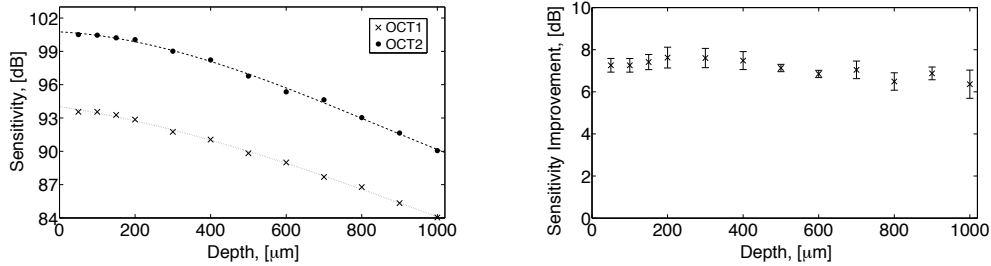


Fig. 6. (a) Measured decay of sensitivity with depth for both OCT configurations. In (b), we have subtracted the two data sets shown in (a) to highlight the improved sensitivity of OCT1 over that of OCT2.

and averaged over 100 spectra, was subtracted to partially remove the DC term present after performing the Fourier Transform (FT) of the signal. The signal was then frequency mapped and resampled to account for the hyperbolic dependence between wavelength and frequency.

Figure 5 shows the sensitivity as a function of reference arm relative reflectivity R_r . The theoretical curves were predicted using Eq. (15). For OCT2, γ_r was 1×10^{-3} , whereas for OCT1 the reference arm efficiency was much higher, $\gamma_r = 78 \times 10^{-3}$. The reference arm power for OCT2 was sufficiently small and only needed a further adjustment of $\Delta\gamma_r = -9.85$ dB to the limited detector dynamic range and saturation level of the chosen camera exposure time. For OCT1, however, in order to operate outside the excess noise regime and to avoid camera saturation, $\Delta\gamma_r$ needed to be optimized to -29 dB. Our measurements agree well with the prediction. The standard deviation of our measurements slightly increases with decreasing reflectivity, which we attribute to the reduced signal to noise ratio and to more prominent noise fluctuations. Clearly the system using the polarization cross talk ratio offers better sensitivity than the standard OCT system.

We have also performed sensitivity measurements for different optical path differences (i.e., depths) for both configurations. As it is well known in FD-OCT, the limited pixel width of the line scan detector induces a signal decay with depth, which results in a loss of sensitivity. This is revealed in Figs. 6(a). The sensitivity improvement for OCT2 over the standard OCT system had a mean value of 7.1 dB [± 0.4 dB], keeping all the other parameters constant between the two configurations. This value is in good agreement with the 7 dB expected theoretically from the factor of 5 increase in the γ_s parameter. As the depth increases, the sensitivity improvement drops slightly below 7 dB. This is explained by several factors. First, the dispersion is not perfectly compensated in OCT2 and there is some residual third order dispersion contributing to a peak broadening and amplitude reduction of the signal. Second, the correlating signals have slightly different spectra because the second PBS in the reference arm is not perfectly designed for our wavelength range. An alternative method to access the p-polarised light from the reference arm, that avoids the need of a second PBS, would be to use a broadband half-wave plate instead of a double pass in a QWP, or to use a corner reflector rather than a flat reference mirror so as to separate the returning beam more readily.

4.2. Acquisition time improvement

The sensitivity improvement of our efficient OCT system can be translated into an enhancement of acquisition speed. Intuitively, sensitivity improvement by a factor of 4 should allow for a reduction of the exposure time by half because of the square root relationship between the exposure time and the interference signal in Eq. (13). However, factoring in the noise contributions, the outcome actually depends on whether the system is receiver-noise, excess-noise,

or shot-noise limited. Eq. (15) indicates that for a receiver-noise limited system, the sensitivity scales as $S \propto \tau^2 \gamma_s \sigma_{\text{rec}}^{-2}$ with exposure time τ , interferometer sample efficiency γ_s , and the receiver noise σ_{rec}^2 , and would indeed lead to the square root relation mentioned above, while for shot noise and excess noise limited systems $S \propto \tau \gamma_s$.

We have investigated the influence of the exposure time on the sensitivity for our efficient OCT configuration (OCT2) both theoretically [Eq. (15)] and experimentally. The results are presented in Figs. 7(a) and (b) as a function of the reference arm reflectivity. Fig. 7(a) shows the theoretically expected sensitivity for two different exposure times, $\tau = 200 \mu\text{s}$ (dashed) and $\tau = 50 \mu\text{s}$ (solid), a four-fold decrease, respectively. The three noise regimes are clearly visible and delineated by labelled straight lines. The vertical lines indicate the CCD saturation level for both exposure times. Subtracting these two curves, we have plotted in Fig. 7(b) the reduction in sensitivity that is expected when the exposure time is reduced by a factor of 4 from $200 \mu\text{s}$ to $50 \mu\text{s}$. Experimental data points are superimposed and found to agree very well with predictions. All the parameters are detailed in the caption. As expected, in the excess-noise limited regime, the exposure time can be reduced by a factor of 4 before the sensitivity is equally reduced by a factor of 4, or 6 dB, and brought down close to the same level as that of the standard OCT configuration (OCT1). In contrast, in the receiver-noise limited regime, the decrease of sensitivity with exposure time is much more dramatic, and the exposure time of OCT2 can only be reduced by a factor of 2 before reaching the sensitivity of OCT1. As OCT normally operates close to saturation, our configuration would normally be within shot-noise limited performance and thus, for equal sensitivity, the acquisition speed of our efficient OCT configuration would be 4 times larger than that of a standard OCT system.

In practice, however, a reduction of exposure time τ is accompanied by a re-optimisation of the reference arm power (or $\Delta\gamma_r$) to keep the camera close to saturation. Figs. 8(a) and (b) present this scenario. The exposure time is reduced by a factor of 4 while, by rotating the QWP, the reference arm power is increased by 6 dB. Here we observe that reducing the exposure time by a factor of 4 actually induces a limited decrease of sensitivity of only 6 dB – 7 dB over the entire detector noise limited regime and, as before, over part of the shot noise regime [compare Fig. 7(b) and 8(b)]. The bump in the graph is due to an exposure-time dependence of the detector noise, $\sigma_{\text{CCD}} = 16e^-$ for $\tau = 50 \mu\text{s}$ and $\sigma_{\text{CCD}} = 15e^-$ for $200 \mu\text{s}$.

It is worth noting that, in the receiver-noise limited regime, the sensitivity $S \propto \tau^2 \gamma_s \sigma_{\text{rec}}^{-2}$ has

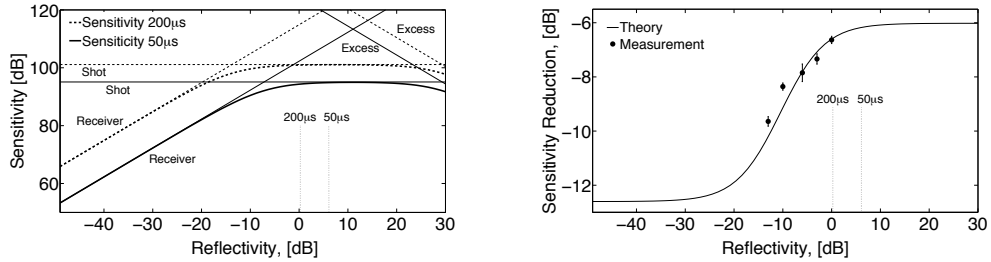


Fig. 7. (a) Theoretical sensitivity of OCT2 predicted from Eq. (15) as a function of the reference arm reflectivity for $\tau = 50 \mu\text{s}$ (solid) and $200 \mu\text{s}$ (dashed). The vertical lines indicate the CCD saturation level for both exposure times and the three different noise regimes are indicated for each sensitivity curve. In (b), we have subtracted the two curves shown in (a) to represent the expected sensitivity reduction due to a four-fold decrease of exposure time and this is compared with experimental data. Other parameters that correspond to the experimental setup are $\gamma_r = 1 \times 10^{-3}$, $\Delta\gamma_r = 1.034 \times 10^{-1}$, $\gamma_s = 0.122$, $\eta = 0.37$, $\rho = 0.11$, $P_0 = 3.2 \text{ mW}$, $\sigma_{\text{CCD}} = 16e^-$ ($15e^-$) for $\tau = 50 \mu\text{s}$ ($200 \mu\text{s}$), $\text{FWC} = 14 \text{ ke}^-$.

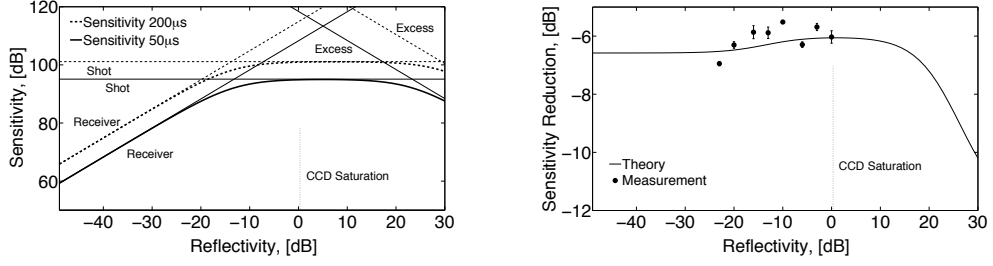


Fig. 8. (a) Theoretical sensitivity of OCT2 predicted from Eq. (15) as a function of the reference arm reflectivity for simultaneous exposure time and saturation adjustment. Dashed curve: $\tau = 200 \mu\text{s}$, $\gamma_r = 1 \times 10^{-3}$, $\Delta\gamma_r = 1.034 \times 10^{-1}$. Solid curve: $\tau = 50 \mu\text{s}$, $\gamma_r = 1 \times 10^{-3}$, $\Delta\gamma_r = 4 \times 1.034 \times 10^{-1}$. (b) Corresponding theoretical and experimental sensitivity reduction when reducing the exposure time [as defined in Fig. 7(b)]. All the other parameters are identical to those of Fig. 7.

a double dependence on the exposure time τ since the receiver noise σ_{rec}^{-2} is also a function of τ . Figure 9 explores this influence theoretically. Here we again present a plot of optimized sensitivity reduction as defined above (Fig. 8), i.e., for a reduction of exposure time by a factor of four combined with an increase in reference arm power by 6 dB. In Figure 9, however, the use of a 3D plot allows us to present the sensitivity reduction as a function of reference arm reflectivity R_r for various factors of change of receiver noise, $\sigma_{\text{rec}2}/\sigma_{\text{rec}1}$, where $\sigma_{\text{rec}1/2}$ are the receiver noise before and after reduction of the exposure time, respectively. In this Figure, the white line corresponds to our experimental conditions where $\sigma_{\text{rec}2}/\sigma_{\text{rec}1} = 1.07$ and is the same as the solid curve of Fig. 8(b). Note how, in the receiver-noise limited regime (i.e., for reference arm reflectivities below -20 dB) the sensitivity reduction varies dramatically with the change in receiver noise. Ideally the receiver noise should be lower for a shorter exposure time, $\sigma_{\text{rec}2}/\sigma_{\text{rec}1} < 1$ and this leads to a comparatively low reduction of sensitivity as the exposure time is decreased. In this condition, the acquisition speed in receiver-noise limited operation can in principle be increased even more without compromising sensitivity (recall that a reduction of sensitivity of 6 dB is equivalent to using a standard OCT configuration, i.e., OCT1). The opposite situation occurs when the receiver noise increases with a decrease of exposure time.

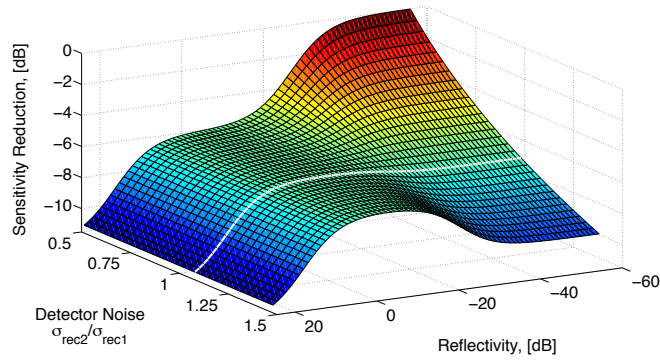


Fig. 9. Sensitivity reduction after exposure time decrease by a factor of four and reference arm power increase by 6 dB as a function of receiver noise ratio, $\sigma_{\text{rec}2}/\sigma_{\text{rec}1}$. The white line shows the case $\sigma_{\text{rec}2}/\sigma_{\text{rec}1} = 1.07$ for our camera settings [Fig. 8 (b)].

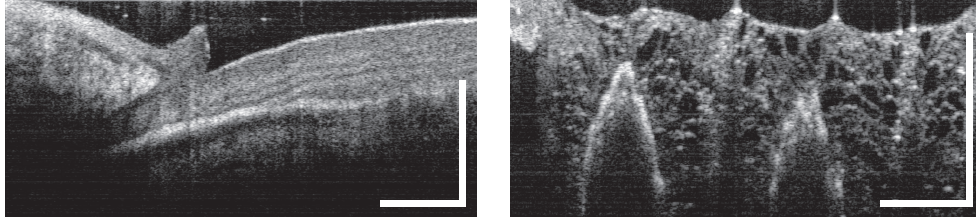


Fig. 10. Cross sectional images of a human nail fold (left) and a kiwifruit (right), using the polarisation cross talk ratio OCT system. Images were recorded at an A-scan rate of 5 kHz and one B-scan contained 877 A-scans and 1,165 A-scans, respectively. The white bars correspond to 1mm.

Note that this dependence on receiver noise becomes irrelevant when operating in the shot noise regime as is the case for our experiment.

We therefore conclude that, for our efficient OCT system, the acquisition speed can be increased by a factor of four while maintaining the same sensitivity performance as for a four-times slower standard OCT configuration. It is important to note that the acquisition time increase is a true information rate increase as defined by Wieser et al. [16].

4.3. Imaging

Finally, for completeness, we present in Figs. 10(a) and (b) OCT images of (a) a human finger nail and (b) a piece of kiwifruit obtained with our polarisation cross talk ratio configuration with a A-scan rate of 5 kHz and a sensitivity of 104 dB. In Fig. 10(a), the birefringence of the finger nail is clearly visible as evidenced by the lines parallel to the nail surface. This could be a disadvantage of our system as the change in optical properties of the sample could be taken for a change in structure, if the birefringent properties of the sample are unknown. However, as can be seen in Fig. 10(b), for non birefringent samples the polarisation sensitive design does not affect the imaging of tissue structure.

5. Conclusion

We have shown that, by using the polarisation crosstalk ratio of a polarising beam splitter, OCT configurations can be made more efficient by using all available source power for the sample arm. The small portion of optical power given by the polarisation crosstalk ratio is used as a reference signal. As a consequence, we avoid operating in the excess intensity noise regime and the sensitivity of such an OCT configuration can be increased by 6 dB. That increase of sensitivity can be converted into an increase of acquisition speed by a factor of 4 for the shot noise optimized configuration. This acquisition time decrease is a true information rate increase. The polarisation sensitivity of the OCT design does not prevent the imaging capabilities of the system.

6. Acknowledgements

The authors would like to Acknowledge Dr Stephane Coen for his useful corrections. This work was supported by the NERF grant from the Foundation for Research Science and Technology from the New Zealand government. This publication is also based on work supported in part by Award No KUK-C1-013-04, made by King Abdullah University of Science and Technology (KAUST).

RECENT REPORTS

44/10	Mud peeling and horizontal crack formation in drying clay	Style Peppin Cocks
45/10	Binocular Rivalry in a Competitive Neural Network with Synaptic Depression	Kilpatrick Bressloff
46/10	A theory for the alignment of cortical feature maps during development	Bressloff Oster
47/10	All-at-Once Solution of Time-Dependent PDE-Constrained Optimisation Problems	Stoll Wathen
48/10	Possible role of differential growth in airway wall remodeling in asthma	Moulton Goriely
49/10	Variational Data Assimilation Using Targetted Random Walks	Cotter Dashti Robinson Stuart
50/10	A model for the anisotropic response of fibrous soft tissues using six discrete fibre bundles	Flynn Rubin Nielsen
51/10	STOCHSIMGPU Parallel stochastic simulation for the Systems Biology Toolbox 2 for MATLAB	Klingbeil Erban Giles Maini
52/10	Order parameters in the Landau-de Gennes theory - the static and dynamic scenarios	Majumdar
53/10	Liquid Crystal Theory and Modelling Discussion Meeting	Majumdar Mottram
54/10	Modeling the growth of multicellular cancer spheroids in a bioengineered 3D microenvironment and their treatment with an anti-cancer drug	Loessner Flegg Byrne Hall Moroney Clements Hutmacher McElwain
55/10	Scalar Z, ZK, KZK, and KP equations for shear waves in incompressible solids	Destradre Goriely Saccomandi
56/10	The Influence of Bioreactor Geometry and the Mechanical Environment on Engineered Tissues	Osborne O'Dea Whiteley Byrne Waters
57/10	A numerical guide to the solution of the bidomain equations of cardiac electrophysiology	Pathmanathan Bernabeu Bordas Cooper

58/10	Particle-scale structure in frozen colloidal suspensions from small angle X-ray scattering	Spannuth Mochrie Peppin Wettlaufer
59/10	Spin coating of an evaporating polymer solution	Munch Please Wagner
60/10	Stochastic synchronization of neuronal populations with intrinsic and extrinsic noise	Bressloff Lai
61/10	Metastable states and quasicycles in a stochastic Wilson-Cowan model of neuronal population dynamics	Bressloff
62/10	Adsorption and desorption dynamics of citric acid anions in soil	Oburger Leitner Jones Zygalakis Schnepf Roose
63/10	A dual porosity model of nutrient uptake by root hairs soil	Zygalakis Kirk Jones Roose Wissuwa
64/10	Hot Charge Pairs and Charge Generation in Donor Acceptor Blends	Kirkpatrick
65/10	Excluded-volume effects in the diffusion of hard spheres	Bruna Chapman
66/10	Dynamics of colloidal particles in ice	Spannuth Mochrie Peppin Wettlaufer

Copies of these, and any other OCCAM reports can be obtained from:

**Oxford Centre for Collaborative Applied Mathematics
Mathematical Institute
24 - 29 St Giles'
Oxford
OX1 3LB
England**

www.maths.ox.ac.uk/occam